RSC Advances

PAPER

View Article Online
View Journal | View Issue

Cite this: *RSC Adv.*, 2025, **15**, 7710

Effect of a polymeric compound layer on jetting dynamics produced by bursting bubbles†

Sainath A. Barbhai,‡[a] Zhengyu Yang ‡[b] and Jie Feng *[b]

Jetting dynamics from bursting bubbles play a key role in mediating mass and momentum transport across the air–liquid interface, and have attracted widespread interest from researchers across disciplines. In marine environments, this phenomenon has drawn considerable attention due to its role in releasing biochemical contaminants, such as extracellular polymeric substances, into the atmosphere through aerosol production. These biocontaminants often exhibit non-Newtonian characteristics, yet the physics of bubble bursting with a rheologically complex layer at the bubble–liquid interface remains largely unexplored. In this study, we experimentally investigate the jetting dynamics of bubble bursting events in the presence of such a polymeric compound layer. Using bubbles coated by a polyethylene oxide solution, we document the cavity collapse and jetting dynamics produced by bubble bursting. At a fixed polymer concentration, the jet velocity increases while the jet radius decreases with an increasing compound layer volume fraction, as a result of stronger capillary wave damping due to capillary wave separation at the compound interface as well as the formation of smaller cavity cone angles during bubble cavity collapse. These dynamics produce smaller and more numerous jet drops. Meanwhile, as the polymer concentration increases, the jet velocity decreases while the jet radius increases for the same compound layer fraction due to the increasing viscoelastic stresses. In addition, fewer jet drops are ejected as the jets become slower and broader with increasing polymer concentration, as viscoelastic stresses persist throughout the jet formation and thinning process. We further obtain, for the first time, a regime map delineating the conditions for jet drop ejection *versus* no jet drop ejection in bursting bubbles coated with a polymeric compound layer. Our results may provide new insights into the mechanisms of mass transport of organic materials in bubble-mediated aerosolization processes, advancing our understanding of marine biology and environmental science.

Received 9th January 2025
Accepted 27th February 2025

DOI: 10.1039/d5ra00228a

rsc.li/rsc-advances

1 Introduction

In nature, countless bubbles are continuously formed through natural physical processes, such as wave breaking,[1] impact of raindrops,[2] and gas release from natural seeps.[3,4] Bubbles are also utilized in a variety of industrial processes involving gas fluxing, such as in bioreactors[5] and wastewater treatment.[6] When these bubbles rise to the air–water interface due to buoyancy, they ultimately burst after the cap film ruptures. The subsequent collapse of the bubble cavity generates capillary waves that converge at the base of the bubble cavity, producing a Worthington jet, which can further disintegrate into smaller jet drops.[7] These drops could transport chemical (sea salts/toxins/microplastics)[1,8–12] and biological (bacteria/virus)[13–15] substances into the atmosphere, impacting climate dynamics, earth system modeling, and public health.[16–19] Therefore, jetting dynamics from bursting bubbles play a vital role in controlling the mass transport across the air–liquid interface, and have received significant attention from researchers across disciplines.[6,10,12–14,20–24]

While most previous studies have focused primarily on clean bubbles, the jetting dynamics of contaminated bubbles have attracted considerable attention only recently. Rising bubbles can scavenge contaminants from biological or industrial origins,[12–14,20,24–29] *e.g.* surfactants, proteins, and biological gels, but their effects on the bubble bursting jets remain largely unexplored. These contaminants are known to modify the interfacial dynamics substantially by altering surface tension and creating surface tension gradients, *i.e.* Marangoni effects, as well as complicating the interfacial rheology. Previous studies have shown the bursting of surfactant-laden bubbles generates fewer jet drops compared to surfactant-free cases due to the suppression of Marangoni stresses.[26,30,31] For bubble bursting at a protein–laden bubble interface, surface elasticity significantly alters the dynamics of cavity collapsing, reducing

[a]*Department of Aerospace Engineering, University of Illinois at Urbana-Champaign, Urbana, USA*

[b]*Department of Mechanical Science and Engineering, University of Illinois at Urbana-Champaign, Urbana, Illinois 61801, USA. E-mail: jiefeng@illinois.edu*

† Electronic supplementary information (ESI) available. See DOI: https://doi.org/10.1039/d5ra00228a

‡ These authors contributed equally to this work.

Table 1 Summary of previous investigations for dynamics of bubble bursting jets in non-Newtonian fluids. The non-dimensional numbers are defined as follows: plastocapillary number ($\mathcal{J}$, the ratio between yield stress and capillary pressure), Deborah number (De; the ratio between the relaxation time of the polymer solution and the inertio-capillary timescale), and elastocapillary number (Ec; the ratio between elastic and capillary stresses). ψ_0 is the volume fraction of the polymeric compound layer of bubbles

Reference	Focus	Fluid rheological model	Important dimensionless numbers
Sanjay, Lohse, and Jalaal[37]	Numer.	Bulk: viscoplastic Bingham model	$0 < \mathcal{J} < 64$
Rodríguez-Díaz *et al.*[38]	Exptl.	Bulk: weakly viscoelastic aqueous PEO solutions	$10^{-7} < \mathrm{De} < 10^{-3}$
Cabalgante-Corralesa *et al.*[39]	Exptl./Numer.	Bulk: viscoelastic Oldroyd-B model	$10^{-3} < \mathrm{De} < 1$, $10^{-3} < \mathrm{Ec} < 10^{-1}$
Dixit *et al.*[40]	Numer.	Bulk: viscoelastic Oldroyd-B model	$10^{-4} < \mathrm{De} < 10^{4}$, $10^{-4} < \mathrm{Ec} < 10^{4}$
Balasubramanian *et al.*[41]	Numer.	Bulk: elastoviscoplastic model by Saramito[42]	$10^{-3} < \mathrm{De} < 30$, $10^{-3} < \mathrm{Ec} < 10$
Current work	Exptl.	Coating compound: weakly viscoelastic aqueous PEO solutions; bulk: Newtonian	$10^{-4} < \mathrm{De} < 10^{-2}$, $10^{-1} < \mathrm{Ec} < 10$, $0 < \psi_0 < 60\%$

jet velocity while increasing jet radius.[27,28] Specifically, biochemical contaminants, such as microbial extracellular polymeric substances (EPSs), may form a viscoelastic layer at the bubble surface due to the three-dimensional network of organic exopolymers.[29,32] Furthermore, EPSs have been identified as one of the key components in marine aerosols ejected by bubble bursting, contributing to cloud condensation nuclei and impacting global radiation.[33–36] Consequently, understanding the influence of non-Newtonian rheology on bubble bursting behavior is essential for advancing our understanding of marine biology and environmental science.

We summarize the recent studies for the effect of non-Newtonian fluid rheology on bubble bursting jets in Table 1. For bare bubble bursting jets in a non-Newtonian fluid, previous numerical investigations have discussed the effect of a viscoplastic,[37] viscoelastic,[40] or elastoviscoplastic[41] medium on the bubble cavity collapse and jet ejection. Specifically, multiple non-dimensional numbers, including the plastocapillary number ($\mathcal{J}$, the ratio between yield stress and capillary pressure), the Deborah number (De, the ratio between the relaxation time of the polymer solution and the inertio-capillary timescale), and the elastocapillary number (Ec, the ratio between elastic and capillary stresses), are used to describe the bulk non-Newtonian rheology. Meanwhile, to the best of our knowledge, systematic experimental investigations in this area remain significantly limited. Using low-molecular-weight polyethylene oxide solutions, Rodríguez-Díaz *et al.*[38] observed that weak viscoelasticity suppresses the ejection of jet drops. A follow-up recent experimental study by Cabalgante *et al.*[39] showed that the polymer viscosity has the largest effect on the jet velocity while the polymer relaxation time affects whether a jet drop is emitted or not. However, previous studies have not explored a widely encountered scenario in nature and industry: compound bubbles coated by a viscoelastic layer similar to EPS. Compared with bare bubble bursting in a non-Newtonian bulk medium, such compound bubbles may result in distinct jetting dynamics, which are more pertinent to the transport and fate of EPS in real oceanic environments, therefore requiring particular attention.

Here, we experimentally investigate the bursting dynamics of compound bubbles coated with a viscoelastic layer, focusing on their jetting dynamics and implications for aerosol generation. We construct our paper as follows: the experimental setup and the rheological characterization for the working fluids are described in Section 2. In Section 3, we analyze the influence of the polymeric compound layer on cavity collapse and the resulting bubble bursting jets, including their corresponding top jet drops. These observations are made across a range of polymer concentrations and compound layer volume fractions, with each parameter quantitatively assessed. Additionally, we discuss the effects of the compound layer on jetting dynamics, particularly considering the non-Newtonian rheology. A regime map is also provided for the first time, illustrating the jet drop/no-jet drop regimes based on variations in polymer concentration and compound layer volume fraction. Finally, we conclude our discoveries and implications of this study in Section 4.

2 Experimental Methodology

2.1 Experimental setup

Fig. 1 shows the schematics of our experimental setup. A co-axial orifice system was used to generate compound bubbles in a controlled way.[43,44] Two syringe pumps (PHD ULTRA and 11 Pico Plus Elite, Harvard Apparatus) were connected to the outer and inner needles with inner diameters of 0.51 mm and 0.16

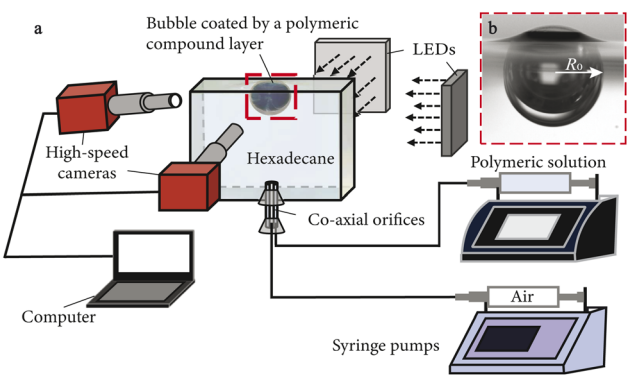

Fig. 1 (a) Experimental setup for high-speed imaging for the jetting dynamics of bubbles with a viscoelastic compound interface. (b) Zoomed-in image of a typical compound bubble coated by a polymeric layer. R_0 is the compound bubble radius.

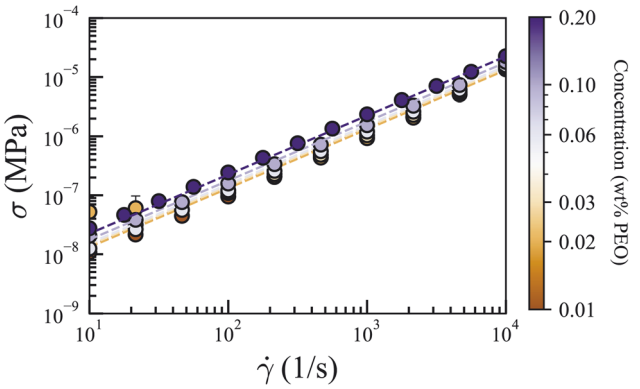

Fig. 2 Shear stress σ as a function of the shear rate $\dot{\gamma}$ for PEO solutions of different concentrations.

mm, respectively, of the orifice system to infuse the polymer solution and air at controlled flow rates. The bubble was released into an acrylic container of dimension 20 × 20 × 25 mm^3, large enough to minimize wall effects on bubble bursting dynamics. A slightly convex meniscus was maintained at the top of the container to keep the coated bubble at the center. Two high-speed cameras (FASTCAM Mini AX200, Photron) were used to synchronously capture the temporal evolution of the cavity collapse and jetting dynamics above and below the free surface, respectively. Both cameras operated at a frame rate of 6400 fps with an image resolution of 5.6–14.3 μm per px. All experiments were conducted with a compound bubble radius of $R_0 = 1.48 \pm 0.11$ mm as shown in Fig. 1. The volume fraction of the compound layer is defined as $\psi_0 = 3V_0/(4\pi R_0^3)$, where we calculate the volume of the compound layer V_0 by image analysis right before jet formation.[45]

2.2 Materials

We used aqueous solutions of polyethylene oxide (PEO) (Sigma-Aldrich, molecular weight of 6×10^5 g mol^{-1}) as the viscoelastic compound layer. The solutions were prepared by dissolving the polymers at a concentration of 0.3 wt% in deionized water (Smart2Pure 3 UV/UF, ThermoFisher Scientific, 18.2 MΩ cm at 20 °C) on a magnetic stirrer for 100 hours, at no heat and low stirring rates to minimize thermal and mechanical degradation.[38] Then the solutions were further diluted to the required PEO concentration for each experiment. All PEO concentrations used in this study are below the critical overlap concentration estimated as 2.44 wt%, which defines the upper limit below which a polymer solution is considered dilute. Above this threshold, polymer chains start to enter a semi-dilute regime to overlap, interact, and may thereafter form entangled networks.[46–48] As shown in Fig. 2, we performed rheological measurements (TA Instruments DHR-3 with a 40 mm diameter and 1° cone plate) and confirmed that PEO solutions used in our experiments can be described as viscoelastic Boger fluids without significant shear thinning.[38,48] To further obtain the apparent extensional relaxation time, we employ the semi-empirical curve fit proposed by Rodríguez-Díaz *et al.* as $\lambda_r = 2.707 \times 10^{-7} c^{1.733}$, where λ_r represents the apparent extensional relaxation time in ms and c denotes the polymer concentration in parts per million (ppm) for PEO.[38,49] Hexadecane (Sigma-Aldrich, Reagent Plus, 99%, density $\rho_b = 773$ kg m^{-3}, dynamic viscosity $\mu_b = 3.45$ mPa s) was used as the Newtonian bulk liquid phase. The interfacial tensions were measured using the pendant drop method and analyzed using the open-source software Opendrop.[50] All the fluid properties are summarized in Table 2.

2.3 Dimensionless numbers

Based on previous numerical investigations for bubble bursting in a bulk non-Newtonian fluid modeled with Oldroyd-B viscoelastic behavior,[39,40] we characterize the non-Newtonian rheological effects with the following dimensionless numbers related to the relaxation time λ_r and the elastic modulus $G = \eta_p/\lambda_r$ of the polymeric solution,[40] respectively. Here, η_p represents the polymer viscosity, calculated as $\eta_p = \eta_t - \eta_s$, where η_t is the total viscosity of the polymeric solution and η_s is the solvent viscosity. Given that the bubble cavity collapse dynamics occur on the order of the inertio-capillary time scale $t_c = \sqrt{\rho_b R_0{}^3/\gamma_e}$, we use the Deborah number $De = \lambda_r/t_c$ to describe the effect of polymer relaxation on the bursting dynamics. Here, ρ_b and R_0 represent bulk liquid density and bubble radius, respectively, and the effective surface tension $\gamma_e = \gamma_{ac} + \gamma_{cb}$ is calculated as the sum of air-compound layer (γ_{ac}) and compound layer-bulk (γ_{cb}) interfacial tensions. Meanwhile, we use the elastocapillary number $Ec = GR_0/\gamma_e$ to characterize the ratio between the elastic and capillary stresses. In addition, the Ohnesorge number that compares the inertial–capillary to inertial–viscous timescales is also considered. Specifically, we introduce the polymeric and solvent Ohnesorge numbers $Oh_p = \eta_p/\sqrt{\rho_c \gamma_e R_0}$ and $Oh_s = \eta_s/\rho_c \gamma_e R_0$ to describe the effects of the polymer and solvent viscosity, respectively, where ρ_c is the compound layer

Table 2 Material properties of the working fluids. Here, η_t is the total viscosity, η_p is the polymer viscosity, λ_r is the extensional relaxation time, γ is the interfacial tension, and the subscripts a, b and c represent air, bulk, and coating compound phases, respectively

PEO concentration, wt%	η_t, mPa s	η_p, mPa s	λ_r, ms	γ_{ac}, mN m^{-1}	γ_{cb}, mN m^{-1}
0.01	1.35 ± 0.02	0.35 ± 0.02	0.001	59.7 ± 0.5	29.8 ± 0.6
0.02	1.32 ± 0.02	0.32 ± 0.02	0.003	61.3 ± 0.5	30.0 ± 0.1
0.03	1.44 ± 0.03	0.44 ± 0.03	0.005	56.9 ± 0.3	28.2 ± 0.1
0.06	1.54 ± 0.08	0.54 ± 0.08	0.018	61.8 ± 0.4	29.7 ± 0.2
0.1	1.77 ± 0.02	0.77 ± 0.02	0.043	61.6 ± 0.4	26.9 ± 0.6
0.2	2.24 ± 0.03	1.24 ± 0.03	0.142	61.1 ± 0.4	29.4 ± 0.3

Table 3 Ranges of non-dimensional numbers in current experiments

PEO concentration, wt%	De	Ec	Oh_p	Oh_s	Oh_t
0.01	1.50×10^{-4}	7.39	9.70×10^{-4}	2.75×10^{-3}	3.72×10^{-3}
0.02	5.02×10^{-4}	1.95	8.59×10^{-4}	2.71×10^{-3}	3.57×10^{-3}
0.03	9.79×10^{-4}	1.44	1.24×10^{-3}	2.81×10^{-3}	4.05×10^{-3}
0.06	3.37×10^{-3}	4.92×10^{-1}	1.46×10^{-3}	2.71×10^{-3}	4.17×10^{-3}
0.1	8.04×10^{-3}	3.02×10^{-1}	2.13×10^{-3}	2.76×10^{-3}	4.89×10^{-3}
0.2	2.70×10^{-2}	1.43×10^{-1}	3.39×10^{-3}	2.73×10^{-3}	6.12×10^{-3}

density. Table 3 lists the calculated dimensionless number for all working fluids. We note that the gravity effect is considered negligible in current experiments given a small Bond number $Bo = \rho_b g R_0^2/\gamma_e$ (ratio between gravity and capillary effects) of ≈ 0.19.

3 Results and discussion

3.1 Cavity collapse and wave propagation

Fig. 3 shows the cavity shape evolution from the cap film breakage ($t = 0$ ms) to the interface reversal, including bare bubble and compound bubble bursting in pure hexadecane. When the bubble cap ruptures, the cavity collapse generates capillary waves that propagate along the air–compound layer interface, contributing to the jet formation ultimately. The capillary waves are progressively damped as they travel down the cavity bottom, substantially affecting the final jet formation. During cavity collapse of a compound bubble, the polymeric compound layer retracts toward the cavity bottom, forming a bulb structure. This retraction behavior is associated with the unfavorable wetting characteristics of the polymeric solution, as verified by the negative spreading coefficient $S = \gamma_{ab} - \gamma_{ac} - \gamma_{cb} < 0$ for all our cases.[51] Here, γ_{ab} is the surface tension of the bulk hexadecane. In addition, at the end of the cavity collapse, we start to observe the entrainment of polymer threads from the collapsing cavity right around jet birth for high PEO concentration and compound layer volume fraction (inset of Fig. 3(c)). The large surface compression during cavity collapse results in the enrichment of the PEO molecules absorbed onto the cavity surface, which get entrained into the compound layer by the extensional flow produced by bubble bursting, similar to the protein fragments shedding from a compressed protein-adsorbed bubble surface reported previously.[28] To investigate the effect of the polymeric compound layer on the cavity

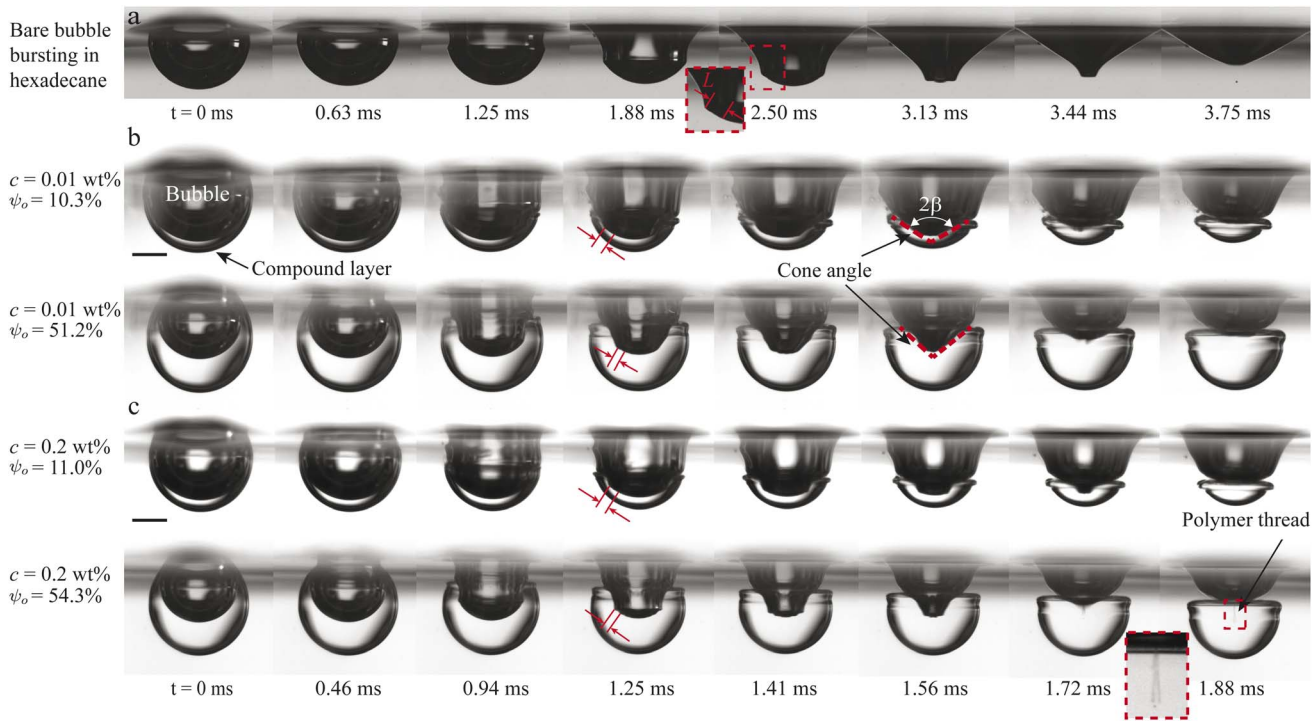

Fig. 3 High-speed imaging of bubble cavity collapse: (a) bare bubble in hexadecane, (b) bubble coated by a compound layer with $c = 0.01$ wt% at $\psi_0 = 10.3\%$ and 51.2%, and (c) bubble coated by a compound layer with $c = 0.2$ wt% at $\psi_0 = 11.0\%$ and 54.3%. The wavelength L was measured between the last two consecutive wave troughs of the capillary wave train. The red dashed lines denote the cone angle of the cavity geometry 2β right before jet formation. The inset in (c) shows a zoom-in view of the polymer thread entrained by bubble bursting flows. All scale bars represent 1 mm. See also ESI Videos 1 and 2† corresponding to (c).

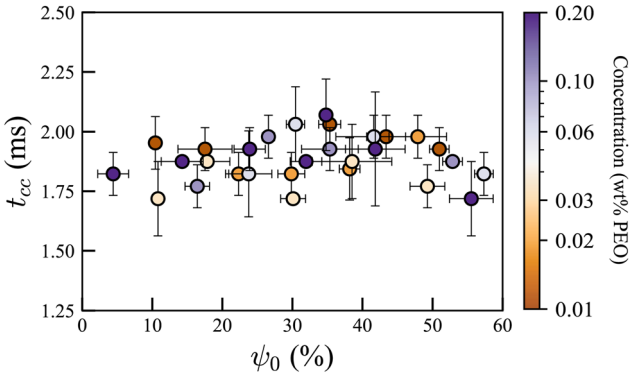

Fig. 4 Cavity collapse time t_{cc} as a function of ψ_0 for bursting bubbles coated by PEO solutions with concentrations of 0.01–0.2 wt%. The collapse time across all cases remains nearly constant, with a value of 1.88 ± 0.11 ms.

collapse behavior, we analyze the capillary wave propagation. A key parameter to characterize the capillary waves is the wavelength L measured between the last two consecutive wave troughs of the capillary wave train.[27,45,52,53] As the characteristic wavelength decreases, the damping of capillary waves is enhanced due to increased viscous dissipation and the separation of capillary waves across the air-compound layer and compound layer-bulk interfaces. It has been shown that the wave separation alters the dispersion relation of the capillary waves, leading to a reduction in L with ψ_0 compared to bare bubble bursting,[45] as we observe in Fig. 3 at approximately $0.25t_c$. Since the viscous damping rate of capillary waves is proportional to L^{-2},[54] this reduction in wavelength significantly amplifies wave damping, resulting in a narrower jet base. To further understand the influence of the polymeric compound layer on the cavity collapse, we also examine the degree to which the cavity forms a cone-like shape right before the jet formation. A geometric dependence has been established in a previous work[55] between the kinematic properties of the jet and the semi-angle of the cavity cone formed when the capillary waves converge at the cavity nadir: the jet velocity increases and the jet radius decreases with the decreased cone angle. Fig. 3(b) and (c) show that the cone angle (defined as 2β) for the higher ψ_0 ($2\beta \approx 100°$, bottom row of Fig. 3(b)) is smaller than that of the lower ψ_0 ($2\beta \approx 117°$, top row of Fig. 3(b)), indicating a progression towards the singular limit of cavity collapse in the former case. We will elaborate in subsequent sections on how the cavity collapse influences the jetting dynamics. Notably, Fig. 4 shows that the cavity collapse time (t_{cc}) remains unchanged as the polymer concentration varies from the lowest ($c = 0.01$ wt%) to the highest ($c = 0.2$ wt%) in the experiments and is also unaffected by the compound layer volume fraction. This is similar to bare bubble bursting in a weakly viscoelastic medium where the cavity collapse time also does not change with polymer concentration.[38–40] The PEO molecules may adsorb onto the interface creating a monolayer due to its surface–active properties. The cavity collapse induces fast fluid motion, which forms a non-uniform surface distribution of PEO molecules and thus gives rise to Marangoni stresses due to surface tension gradient. Previous experimental and numerical studies[26,31,56] demonstrated that the Marangoni stresses from surfactant solutions slow down bubble cavity collapse by opposing the capillary wave propagation. In addition, the interfacial elasticity of an adsorbed protein monolayer has also been found to retard the cavity collapse and increase the cavity collapse time as well.[28] However, we observe an approximately constant cavity collapse time t_{cc} across the investigated range of coating fractions and polymer concentrations, suggesting that Marangoni stresses and interfacial rheology do not significantly influence the cavity collapse and jetting dynamics in current experiments with $10^{-4} < De < 10^{-2}$, $10^{-1} < Ec < 10$, $0 < \psi_0 < 60\%$.

3.2 Jetting dynamics

Following the cavity collapse and focusing of capillary waves at the cavity bottom, jet ejection occurs with the reversal of the bottom curvature as shown in Fig. 5 and 6 from systematically controlled experiments varying with both the compound layer volume fraction ψ_0 and polymer concentration c. The rising Worthington jets primarily consist of polymer solutions, which undergo substantial extensional deformation during their formation and ascent. Due to the Rayleigh–Plateau instability, the jets break into drops, each connected by a viscoelastic filament that ultimately ruptures, releasing the drops. As ψ_0 increases while the polymer concentration c maintains constant, a comparison among Fig. 5(a)–(c) reveals that the jet grows thinner and faster, producing drops noticeably smaller and of a larger number. Additionally, a characteristic "beads-on-a-string" structure emerges in the cases with drop formation. The persistent liquid filament between the droplets indicates that viscoelastic stresses play a significant role in inhibiting the thinning of the liquid bridge,[57] revealing the polymeric solution's strong influence on jet evolution. During the jet rise, the viscoelastic filament undergoes tensile stretching while connecting drops for a prolonged time until its eventual breakup, which leads to the ejection of jet drops. The number of drops increases with ψ_0 for a given c. As the polymer concentration c increases for a specific ψ_0, as shown in Fig. 6(a)–(c) the jet becomes thicker and weaker, showing a stronger inhibition on the jet ejection with increasing viscoelastic effect. Fewer or even no drops are produced due to the widening of the jet shape. In all experimental cases, the viscoelastic compound layer fluid is consistently entrained into the jet. In cases where drop ejection occurs, jet drops are predominantly composed of the compound layer fluid and coated with a thin layer of the bulk Newtonian fluid. Furthermore, at higher polymer concentrations ($c \geq 0.2$ wt%), jet drop formation is completely suppressed, and only a rising jet containing the compound layer fluid is observed.

We further measure the nondimensionalized jet velocity v_j/v_{ce} and nondimensionalized jet radius r_j/R_0 as a function of the compound layer volume fraction ψ_0 at different PEO concentrations, as shown in Fig. 7. Here, jet velocity v_j is non-dimensionalized by the capillary velocity $v_{ce} = \sqrt{\gamma_e/(\rho_b R_0)}$, and jet radius r_j is non-dimensionalized by the compound bubble radius R_0. We measured the jet velocity and radius, both when

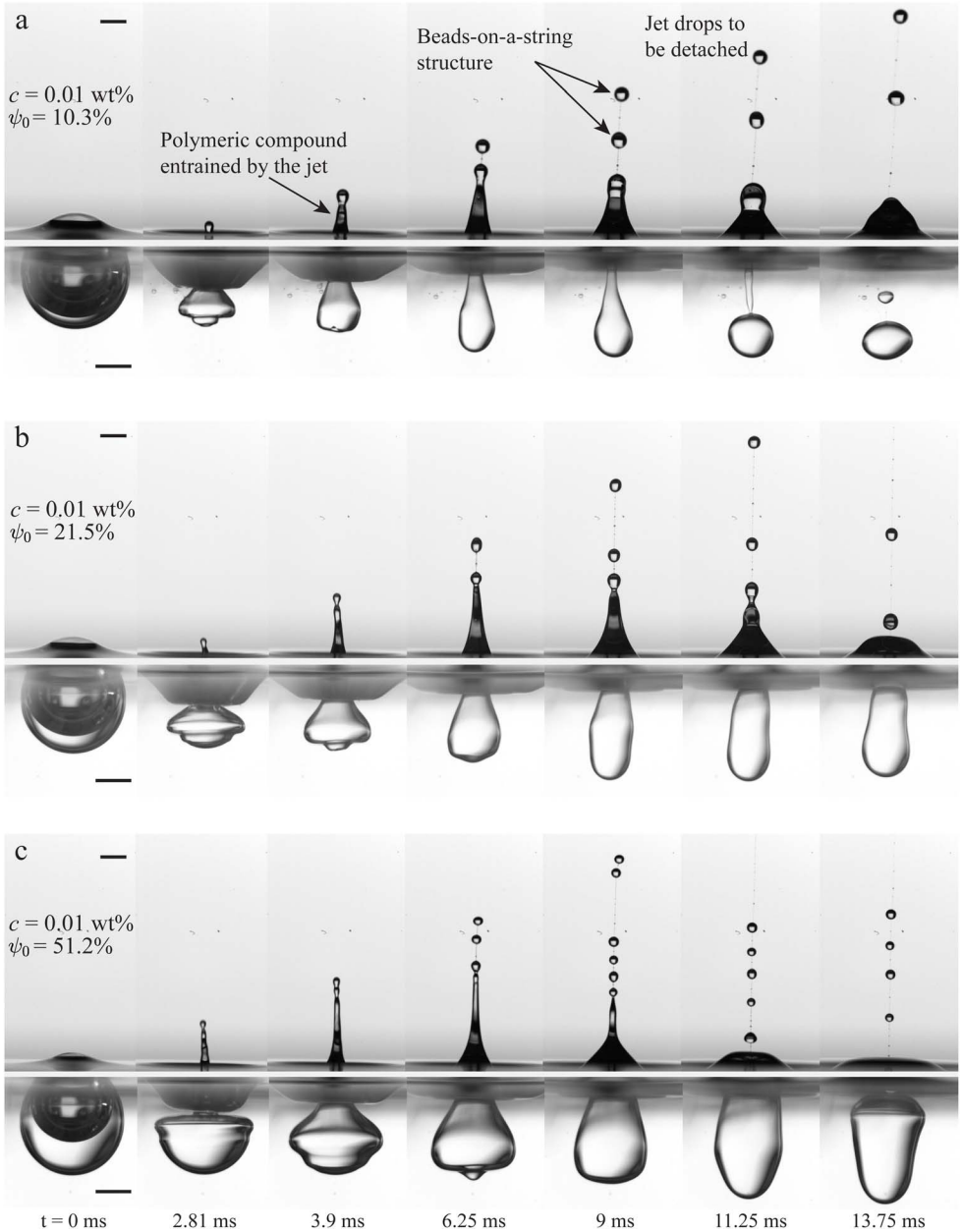

Fig. 5 Side view of a bursting bubble coated by a compound layer at a PEO concentration of 0.01 wt% for (a) $\psi_0 = 10.3\%$, (b) $\psi_0 = 21.5\%$, and (c) $\psi_0 = 51.2\%$. During the rising of the jet, the end-pinching instability causes it to break up into drops and form a beads-on-a-string structure. All scale bars represent 1 mm. See also ESI Videos 3 and 4† corresponding to (a).

the jet tip crosses the undisturbed bulk free surface level. Compared to the bare bubble bursting case with a similar bubble radius, the dimensionless jet velocities produced by compound bubble bursting cases are smaller, while the dimensionless jet radii are larger. This observation signifies that the viscoelastic compound layer on a bubble suppresses the jet ejection compared to the bare bubble case, highlighting the necessity of understanding the role of viscoelastic effects in bubble-bursting jet formation.

When the compound layer volume fraction ψ_0 increases for a constant polymer concentration c, we observe that v_j increases while r_j decreases, until they plateau at $\psi_0 \geq 30\%$. The increase in jet velocity as a function of ψ_0 for the same c is attributed to the enhancement of the jet due to the damping of short-wavelength precursor capillary waves during cavity collapse. Larger ψ_0 results in smaller characteristic wavelength as a thicker compound layer decreases the wavelength L more significantly due to earlier and stronger wave separation,[45] leading to less short-wavelength perturbation for the focusing of the capillary waves at the cavity nadir which allows the formation of a faster and thinner jet. Additionally, capillary wave focusing at a higher ψ_0 produces a cavity with a lower cone angle, 2β, for the same c, as showcased in Fig. 3. Such smaller cone angle has been shown to favor the production of narrower jets with a faster speed in previous theoretical and simulation

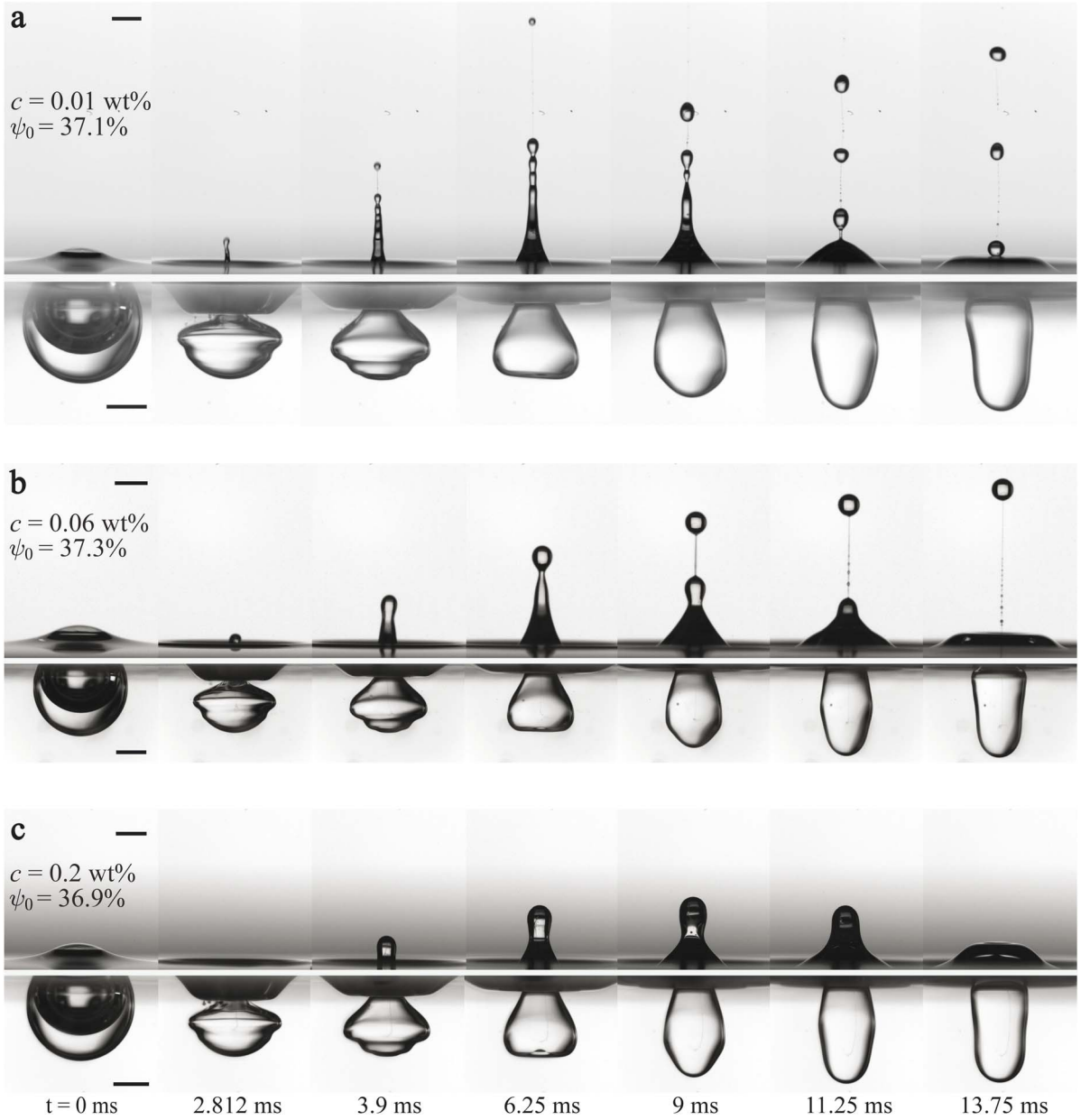

Fig. 6 Side view of a bursting bubble coated by a compound layer at a PEO concentration of (a) $c = 0.01$ wt%, (b) $c = 0.06$ wt%, and (c) $c = 0.2$ wt% for $\psi_0 \approx 37\%$. As c increases while maintaining a nearly constant ψ_0, we observe a transition in compound bubble bursting behavior from generating jet drops to producing no jet drops. All scale bar represents 1 mm.

investigation,[55] which is also consistent with the enhancement of jetting observed in our experiments.

Meanwhile, v_j/v_{ce} decreases and r_j/R_0 increases significantly with PEO concentration, while Oh_t remains relatively constant. As PEO concentration increases from 0.01 wt% to 0.2 wt%, De increases by two orders of magnitude from 1.50×10^{-4} to 2.70×10^{-2}. The substantial increase in polymer relaxation time suggests enhanced viscoelastic effects. The stronger viscoelastic effect of the compound layer leads to a thicker, slower, and wider jet with a reduced final height, which is consistent with similar studies of bubble bursting in viscoelastic liquids.[38–40]

In essence, at the moment of jet formation in the polymeric compound layer, the axial strain rate and viscoelastic stresses at the jet base increase due to polymer stretching caused by the extensional flow. As De increases, the extensional thickening is strengthened by increased elasticity due to higher polymer concentrations.

3.3 Velocity and radius of top jet drops

At the end stages of the jetting, we observe that drops pinch off from the end of the jet due to Rayleigh–Plateau instability. The pinched-off drops form filaments between them and the main jet due to the transition from an inertio-capillary regime to the elastocapillary regime.[39,58] The elastocapillary thinning of these filaments, driven by the tensile forces exerted by the ejecting drops, gives rise to the characteristic "bead-on-a-string"

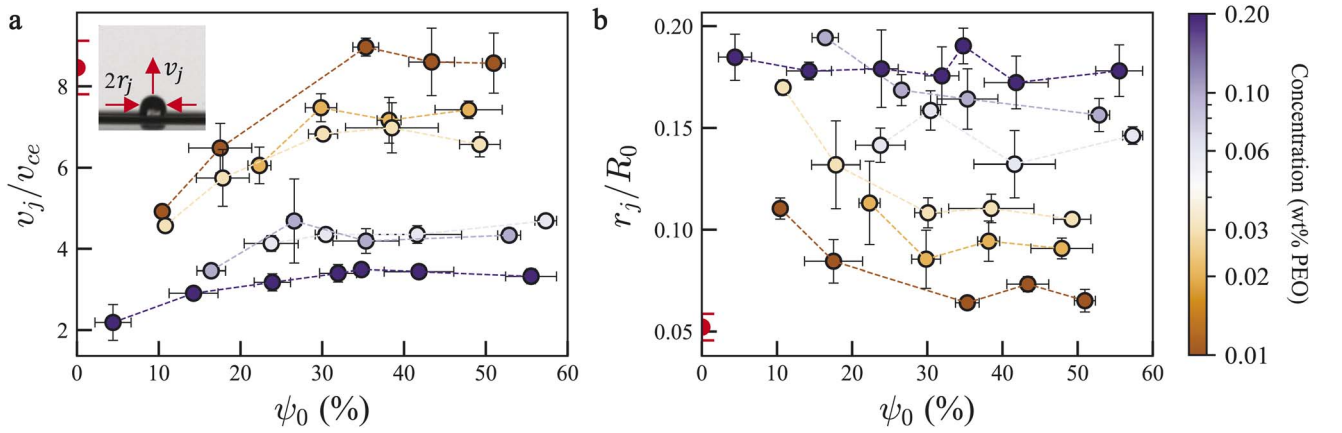

Fig. 7 Non-dimensionalized jet (a) velocity and (b) radius as functions of compound layer volume fraction for bubble bursting with PEO concentrations of 0.01–0.2 wt%. Red markers and error bars on the *Y*-axis denote the case of bare bubble bursting in hexadecane, with a bubble radius similar to that of a compound bubble.

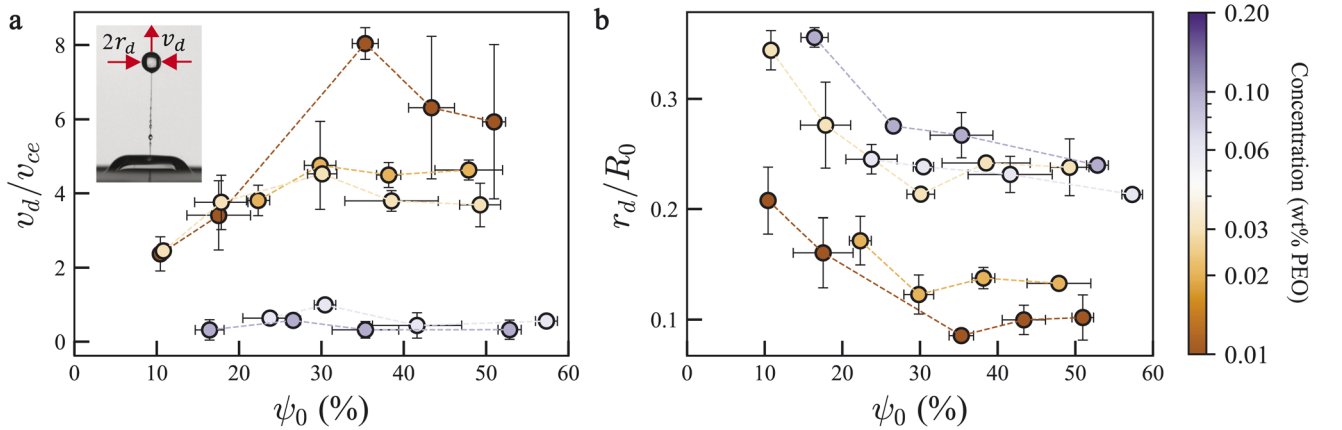

Fig. 8 Non-dimensionalized top jet drop (a) velocity and (b) radius as a function of compound layer volume fraction with PEO concentrations of 0.01–0.1 wt% under which jet drops form.

structure. This filament-thinning is primarily governed by the interplay of surface tension and elasticity, persisting until the filament breaks and releases the drops. In Fig. 8, we show the dimensionless velocity v_d/v_{ce} and radius r_d/R_0 of the top drop as a function of ψ_0. The velocity and radius of the top jet drop are measured when the filament thins to a critical threshold (~30 μm). The drop velocity increases and radius decreases for increasing ψ_o and decreasing c, a consistent trend with that of the jet velocity and radius. Additionally, for the lowest polymer concentrations c, the velocity of the drop v_d almost matches the jet velocity v_j, indicating minor influence from polymer filament stretching as $De \sim \mathcal{O}(10^{-4})$. However, for higher concentrations, a noticeable difference between v_d and v_j emerges. The difference between v_j/v_{ce} to v_d/v_{ce} increases from 2.2 to 3.8 in average as c increases from 0.01 wt% to 0.1 wt%, demonstrating the significant viscoelastic effect with increasing De. The decrease in the jet velocity during the jet growth is due to the viscoelastic tensile stresses developing during the evolution of the jet. During the jet growth before the top jet drop forms, the extensional strain rate at the jet base and near the jet tip could exceed the threshold for polymer coil–stretch transition, causing a significant increase in extensional polymeric stress which slows down the jet.[39] At the initial stage of drop formation, the velocity of the top jet drop matches the velocity of its

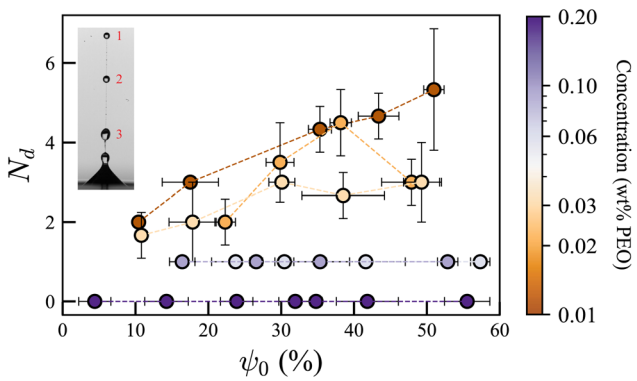

Fig. 9 Number of jet drops, N_d, as a function of compound layer volume fractions with different PEO concentrations of 0.01–0.2 wt%. The inset illustrates an example featuring three jet drops.

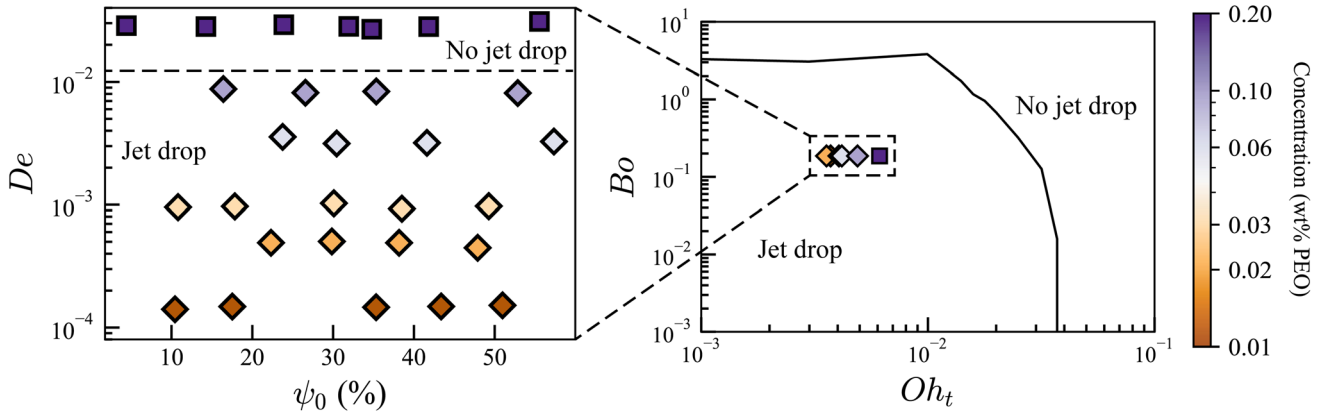

Fig. 10 Regime maps depicting jet-drop and no-jet-drop transitions for jets from bursting bubbles with a viscoelastic compound layer (left) and bare bubbles (right). The left figure demonstrates the jet drop behavior in a De $-$ ψ_0 space. Here, the diamond markers indicate the production of jet drops, the square markers indicate the absence of jet drops, and the dashed line indicates the experimentally observed regime boundary. The right figure demonstrates the projection of the experiments onto the parametric space of Bo and Oh_t. The jet-drop and no-jet-drop regimes are reproduced from a previous study of bare bubble bursting.[60]

jet. However, the drops decelerate from the initial velocity over time due to the pulling force from the thinning filament. As De increases, a larger pulling force is exerted by the filament and decelerates the drop before its final detaching, which ultimately accounts for the significant difference between v_d and v_j at higher c. This can be evidenced by comparing Fig. 6(a) and (b), as the viscous filament for $c = 0.06$ wt% maintains thicker and relaxes slower compared to those for $c = 0.01$ wt%, stretching on the ejected drops. The radius of the ejected drops r_d, which are determined by the breakup dynamics of the jet and influenced by the jet rheological properties, similarly increases significantly for cases with higher PEO concentration and De.

3.4 Number of the jet drops

We observe a systematic dependence of the number of jet drops (N_d) produced on ψ_0 for different polymer concentrations, as illustrated in Fig. 9. Here, we account for all drops generated during bubble bursting, regardless of whether they detach from the thinning filament. The most significant trend is the increase of N_d with ψ_0 for $c < 0.06$ wt%. This is due to the effect of jet enhancement with increasing ψ_0 that results in higher v_j, for which thinner and more slender jet permits the formation of more drops. For $c = 0.06$ or 0.1 wt%, $N_d = 1$ stays constant. A transition from a drop-producing regime to a no-jet-drop regime is observed as c continues to increase, with drop ejection ceasing entirely at $c = 0.2$ wt% for all ψ_0 values. Additionally, we observe an overall decrease of N_d with c. In cases with $c <$ 0.06 wt%, multiple drops form, with the initial drops ejected upward and completely detaching after filament thinning, while the remaining drops, lacking sufficient velocity to overcome the filament's retraction force, are pulled back into the bulk fluid. For cases where 0.06 wt% $\leq c \leq$ 0.1 wt%, only a single drop is ejected, and it is eventually pulled back into the bulk for $c =$ 0.1 wt%. The decrease of N_d is attributed to the increased viscoelastic effect. As previously discussed, larger De results in a thicker filament due to a higher amount of polymer solution being entrained by the rising jet, leading to larger drop radii. The number of jet drops is governed by the pinching dynamics of the jet.[59] Stronger viscoelasticity causes slower and thicker jets, allowing fewer spaces for drops to be generated from the Rayleigh–Plateau mechanism.

3.5 Regime map for bubble bursting jet drops

Based on the above results, we demonstrate a regime map of whether jet drops will be produced, as shown in Fig. 10. When comparing our compound bubble bursting cases with the previously reported Oh–Bo regime map for jet drop production in bare bubble bursting[60] (Fig. 10 (Right)), current experiments fall within the predicted Newtonian jet drop region, including the no-jet-drop cases at the highest polymer concentration of c $= 0.2$ wt%. The difference highlights that the effect of a viscoelastic compound layer could profoundly modify the jetting dynamics. We plot the regime map for jet drop production regarding the important dimensionless parameters in our experiments, De and ψ_0 (Fig. 10 (Left)). Notably, for the first time, we show that compound bubble bursting transitions into a no-jet-drop regime for De $\gtrsim 10^{-2}$, where the ejected jet no longer produces jet drops. This is due to the relaxation time being sufficiently high to induce substantial polymeric stresses, leading to a corresponding increase in extensional viscosity. As a result, more of the polymeric coating is entrained, ultimately slowing down the jet and suppressing drop ejection in the short period of jet rising before it falls back to the pool. In addition, this upper bound of De for jet drop ejection is similar to the value for bare bubble bursting in a viscoelastic fluid,[38,39] since the jet from compound bubble bursting primarily consists of the polymeric coating. We note that ψ_0 has negligible influence on the transition from jet-drop to no-jet-drop regimes in the current experiments.

4 Conclusions

In conclusion, we experimentally investigated the dynamics of bubble bursting with a polymeric compound layer in a Newtonian

fluid. By systematically varying the compound layer volume fraction and polymer concentration, we explored their impact on cavity collapse and jetting behavior. During the bursting of such a compound bubble, bubble cavity collapses with capillary waves focusing at the bottom, ejecting a jet that entrains the viscoelastic compound layer fluid into the atmosphere.

We first find that the presence of the compound layer has negligible influence on the cavity collapse timescale, regardless of the polymer concentration or the compound layer volume fraction. Next, we observe a more slender jet with faster velocity and smaller radius when the compound layer volume fraction increases. We attribute the more energetic jet to the damping of capillary waves and the decrease of cavity cone angle before jet birth. Moreover, despite the nearly constant Oh_t number across the polymer concentrations in our experiments, we observe a decrease in jet velocity and an increase in jet radius with increasing polymer concentration. This is due to the increasing viscoelasticity that introduces strong extensional stresses slowing down the stretching jet. When De is smaller than 10^{-2}, the ejected jet breaks down into drops connected by elastocapillary filaments, which gradually thin due to tensile stretching. This process closely resembles the characteristic "beads-on-a-string" structure for viscoelastic liquid thread thinning. Additionally, this viscoelastic filament exerts a drag force on the drops formed, decelerating their velocity more strongly at higher polymer concentrations with a longer polymer relaxation time. As the polymer concentration rises, De increases and the number of drops decreases. The production of jet drops eventually ceases entirely at a polymer concentration of 0.2 wt%. Additionally, the number of drops formed increases with the compound layer volume fraction for a given polymer concentration as the jet becomes more slender. We also provide a regime map across a range of De and ψ_0, illustrating the conditions under which jet drops are produced or suppressed in compound bubble bursting.

We believe that our findings advance the understanding of fluid mechanics and interfacial transport governing the bursting of bubbles coated with rheologically complex contaminants. Furthermore, this study may offer valuable insights into the ocean-atmosphere mass transport of biochemical substances mediated by bubble bursting, which plays a critical role in marine biology and environmental science.

Data availability

The graphical and high-speed imaging data presented in the manuscript will be available on request. All details are mentioned in the manuscript.

Author contributions

S. B.: data curation; investigation; formal analysis; methodology; visualization; validation; writing – original draft; and writing – review & editing. Z. Y.: Data curation; investigation; validation; and writing – review & editing. J. F.: conceptualization; funding acquisition; formal analysis; investigation; project administration; resources; supervision; and writing – review & editing.

Conflicts of interest

There are no conflicts to declare.

Acknowledgements

We thank the Materials Research Laboratory (MRL) at the University of Illinois at Urbana-Champaign for granting access to their stress-controlled rheometer for partial characterization of the polymer solutions. We also acknowledge Prof. Randy H. Ewoldt and Prof. Jonathan Freund at the University of Illinois at Urbana-Champaign for their valuable discussions and insights. S. B., Z. Y., and J. F. acknowledge partial support by the National Science Foundation (NSF) under grants no. CBET 2426809, 2323045 and the research support award RB24105 from the Campus Research Board at the University of Illinois at Urbana-Champaign.

Notes and references

1 L. Deike, *Annu. Rev. Fluid Mech.*, 2022, **54**, 191–224.
2 S. T. Thoroddsen, K. Takehara, H. Nguyen and T. Etoh, *J. Fluid Mech.*, 2018, **848**, R3.
3 C. Johansen, A. C. Todd and I. R. MacDonald, *Mar. Petrol. Geol.*, 2017, **82**, 21–34.
4 C. Johansen, L. Macelloni, M. Natter, M. Silva, M. Woosley, A. Woolsey, A. Diercks, J. Hill, R. Viso, E. Marty, et al., *Earth Planet. Sci. Lett.*, 2020, **545**, 116411.
5 D. D. McClure, J. M. Kavanagh, D. F. Fletcher and G. W. Barton, *Chem. Eng. Sci.*, 2016, **144**, 58–74.
6 M. Sakr, M. M. Mohamed, M. A. Maraqa, M. A. Hamouda, A. A. Hassan, J. Ali and J. Jung, *Alex. Eng. J.*, 2022, **61**, 6591–6612.
7 L. Deike, E. Ghabache, G. Liger-Belair, A. K. Das, S. Zaleski, S. Popinet and T. Séon, *Phys. Rev. E*, 2018, **3**, 013603.
8 E. R. Lewis and S. E. Schwartz, *Sea Salt Aerosol Production: Mechanisms, Methods, Measurements, and Models*, American Geophysical Union, Washington, DC, 2004, vol. 152.
9 C. Textor, M. Schulz, S. Guibert, S. Kinne, Y. Balkanski, S. Bauer, T. Berntsen, T. Berglen, O. Boucher, M. Chin, et al., *Atmos. Chem. Phys.*, 2006, **6**, 1777–1813.
10 F. Veron, *Annu. Rev. Fluid Mech.*, 2015, **47**, 507–538.
11 N. E. Olson, M. E. Cooke, J. H. Shi, J. A. Birbeck, J. A. Westrick and A. P. Ault, *Environ. Sci. Technol.*, 2020, **54**, 4769–4780.
12 D. B. Shaw, Q. Li, J. K. Nunes and L. Deike, *PNAS Nexus*, 2023, **2**, pgad296.
13 S. Poulain and L. Bourouiba, *Phys. Rev. Lett.*, 2018, **121**, 204502.
14 D. C. Blanchard, *Estuaries*, 1989, **12**, 127–137.
15 O. McRae, K. R. Mead and J. C. Bird, *Phys. Rev. E*, 2021, **6**, L031601.
16 T. W. Wilson, L. A. Ladino, P. A. Alpert, M. N. Breckels, I. M. Brooks, J. Browse, S. M. Burrows, K. S. Carslaw, J. A. Huffman, C. Judd, et al., *Nature*, 2015, **525**, 234–238.

17 B. Néel, M. Erinin and L. Deike, *Geophys. Res. Lett.*, 2022, **49**, e2021GL096740.
18 L. Bourouiba, *Annu. Rev. Fluid Mech.*, 2021, **53**, 473–508.
19 L. Bourouiba, *Annu. Rev. Biomed. Eng.*, 2021, **23**, 547–577.
20 D. Tammaro, V. Chandran Suja, A. Kannan, L. D. Gala, E. Di Maio, G. G. Fuller and P. L. Maffettone, *Proc. Natl. Acad. Sci. U. S. A.*, 2021, **118**, e2105058118.
21 K.-H. Chen, Y.-B. Miao, C.-Y. Shang, T.-Y. Huang, Y.-T. Yu, C.-N. Yeh, H.-L. Song, C.-T. Chen, F.-L. Mi, K.-J. Lin, et al., *Biomaterials*, 2020, **255**, 120157.
22 R. Zenit and J. Rodríguez-Rodríguez, *Phys. Today*, 2018, **71**, 44–50.
23 J. Saththasivam, K. Loganathan and S. Sarp, *Chemosphere*, 2016, **144**, 671–680.
24 T.-B. Robinson, O. Wurl, E. Bahlmann, K. Jürgens and C. Stolle, *Limnol. Oceanogr.*, 2019, **64**, 2358–2372.
25 B. Ji, A. Singh and J. Feng, *Nano Lett.*, 2022, **22**, 5626–5634.
26 C. R. Constante-Amores, L. Kahouadji, A. Batchvarov, S. Shin, J. Chergui, D. Juric and O. K. Matar, *J. Fluid Mech.*, 2021, **911**, A57.
27 Z. Yang, S. Barbhai, B. Ji and J. Feng, *Soft Matter*, 2024, 4868–4877.
28 B. Ji, Z. Yang, Z. Wang, R. H. Ewoldt and J. Feng, *Phys. Rev. Lett.*, 2023, **131**, 104002.
29 A. W. Decho and T. Gutierrez, *Front. Microbiol.*, 2017, **8**, 922.
30 J. Pierre, M. Poujol and T. Séon, *Phys. Rev. E*, 2022, **7**, 073602.
31 P. Pico, L. Kahouadji, S. Shin, J. Chergui, D. Juric and O. K. Matar, *Phys. Rev. E*, 2024, **9**, 083606.
32 M. M. Mrokowska and A. Krztoń-Maziopa, *Sci. Rep.*, 2019, **9**, 7897.
33 E. K. Bigg, *Environ. Chem.*, 2007, **4**, 155–161.
34 E. K. Bigg and C. Leck, *J. Geophys. Res. Atmos.*, 2008, **113**, D11209.
35 C. Leck and E. Keith Bigg, *Tellus B*, 2008, **60**, 118–126.
36 M. Kuznetsova, C. Lee and J. Aller, *Mar. Chem.*, 2005, **96**, 359–377.
37 V. Sanjay, D. Lohse and M. Jalaal, *J. Fluid Mech.*, 2021, **922**, A2.
38 P. Rodríguez-Díaz, A. Rubio, J. Montanero, A. Gañán-Calvo and M. Cabezas, *Phys. Fluids*, 2023, **35**, 102107.
39 E. Cabalgante-Corrales, B. Muñoz-Sánchez, J. López-Herrera, M. Cabezas, E. Vega and J. Montanero, *Int. J. Multiphase Flow*, 2024, 105095.
40 A. K. Dixit, A. Oratis, K. Zinelis, D. Lohse and V. Sanjay, *arXiv*, 2024, preprint, arXiv:2408.05089, DOI: **10.48550/arXiv.2408.05089**.
41 A. G. Balasubramanian, V. Sanjay, M. Jalaal, R. Vinuesa and O. Tammisola, *arXiv*, 2024, preprint, arXiv:2409.14897, DOI: **10.48550/arXiv.2409.14897**.
42 P. Saramito, *J. Non-Newtonian Fluid Mech.*, 2007, **145**, 1–14.
43 B. Ji, Z. Yang and J. Feng, *Phys. Rev. E*, 2021, **6**, 033602.
44 B. Ji, A. Singh and J. Feng, *Phys. Fluids*, 2021, **33**, 103316.
45 Z. Yang, B. Ji, J. T. Ault and J. Feng, *Nat. Phys.*, 2023, **19**, 884–890.
46 V. Tirtaatmadja, G. H. McKinley and J. J. Cooper-White, *Phys. Fluids*, 2006, **18**, 043101.
47 F. Del Giudice, S. J. Haward and A. Q. Shen, *J. Rheol.*, 2017, **61**, 327–337.
48 D. F. James, *Annu. Rev. Fluid Mech.*, 2009, **41**, 129–142.
49 M. Rubio, A. Ponce-Torres, E. J. Vega and J. M. Montanero, *Materials*, 2020, **13**, 192.
50 E. Huang, A. Skoufis, T. Denning, J. Qi, R. R. Dagastine, R. F. Tabor and J. D. Berry, *J. Open Source Softw.*, 2021, **6**, 2604.
51 P.-G. de Gennes, F. Brochard-Wyart, D. Quéré, P.-G. de Gennes, F. Brochard-Wyart and D. Quéré, *Capillarity: Deformable Interfaces*, Springer, New York, 2004, pp. 1–31.
52 S. Krishnan, E. J. Hopfinger and B. A. Puthenveettil, *J. Fluid Mech.*, 2017, **822**, 791–812.
53 J. M. Gordillo Arias de Saavedra and J. Rodríguez Rodríguez, *J. Fluid Mech.*, 2019, **867**, 556–571.
54 G. K. Batchelor, *An Introduction to Fluid Dynamics*, Cambridge university press, Cambridge, 2000.
55 J. M. Gordillo and F. J. Blanco-Rodríguez, *Phys. Rev. E*, 2023, **8**, 073606.
56 E. J. Vega and J. M. Montanero, *Exp. Therm. Fluid Sci.*, 2024, **151**, 111097.
57 C. Clasen, J. Eggers, M. A. Fontelos, J. Li and G. H. McKinley, *J. Fluid Mech.*, 2006, **556**, 283–308.
58 U. Sen, D. Lohse and M. Jalaal, *arXiv*, 2022, preprint, arXiv:2207.07928, DOI: **10.48550/arXiv.2207.07928**.
59 A. Berny, L. Deike, S. Popinet and T. Séon, *Phys. Rev. E*, 2022, **7**, 013602.
60 P. L. Walls, L. Henaux and J. C. Bird, *Phys. Rev. E*, 2015, **92**, 021002.